Joining Time-Resolved Thermometry and Magnetic-Induced Heating in a Single Nanoparticle Unveils Intriguing Thermal Properties

Rafael Piñol,[†] Carlos D. S. Brites,[‡] Rodney Bustamante,[†] Abelardo Martínez,[§] Nuno J. O. Silva,[‡] José L. Murillo,[†] Rafael Cases,[†] Julian Carrey,[‖] Carlos Estepa,[†] Cecilia Sosa,[⊥] Fernando Palacio,[†] Luís D. Carlos,[*,‡] and Angel Millán[*,†]

[†]Departamento de Fisica de la Materia Condensada, Facultad de Ciencias and Instituto de Ciencia de Materiales de Aragón, CSIC—Universidad de Zaragoza, 50009 Zaragoza, Spain, [‡]Departamento de Física and CICECO Aveiro Institute of Materials, Universidade de Aveiro, 3810—193 Aveiro, Portugal, [§]Departamento de Electrónica de Potencia. I3A, Universidad de Zaragoza, 50018 Zaragoza, Spain, [‖]Laboratoire de Physique et Chimie des Nano-Objets (LPCNO)Université de Toulouse, INSA, UPS, CNRS (UMR 5215), F-31077, Toulouse, France, and [⊥]Departamento de Toxicología, Facultad de Veterinaria, Universidad de Zaragoza, 50013 Zaragoza, Spain

ABSTRACT Whereas efficient and sensitive nanoheaters and nanothermometers are demanding tools in modern bio- and nanomedicine, joining both features in a single nanoparticle still remains a real challenge, despite the recent progress achieved, most of it within the last year. Here we demonstrate a successful realization of this challenge. The heating is magnetically induced, the temperature readout is optical, and the ratiometric thermometric probes are dual-emissive Eu^{3+}/Tb^{3+} lanthanide complexes. The low thermometer heat capacitance ($0.021 \cdot K^{-1}$) and heater/thermometer resistance ($1\ K \cdot W^{-1}$), the high temperature sensitivity ($5.8\% \cdot K^{-1}$ at 296 K) and uncertainty (0.5 K), the physiological working temperature range (295—315 K), the readout reproducibility (>99.5%), and the fast time response (0.250 s) make the heater/thermometer nanoplatform proposed here unique. Cells were incubated with the nanoparticles, and fluorescence microscopy permits the mapping of the intracellular local temperature using the pixel-by-pixel ratio of the Eu^{3+}/Tb^{3+} intensities. Time-resolved thermometry under an ac magnetic field evidences the failure of using macroscopic thermal parameters to describe heat diffusion at the nanoscale.

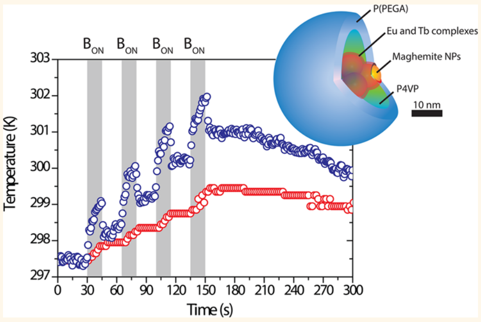

KEYWORDS: nanothermometers · nanoheaters · magnetic hyperthermia · intracellular temperature · heat diffusion

Nanothermometers, nanoheaters, and nanoscale heat transfer are hot topics in nanotechnology.[1−3] These three fields are interrelated and depend on each other for their parallel development. A detailed understanding of heat propagation processes at the nanoscale requires the development of thermometric and heating tools with nanometric resolution.[3−5] Magnetic-, plasmonic-, and phonon-induced thermal heating of nanoparticles are powerful noninvasive techniques for bio- and nanotechnology applications, such as drug release,[6,7] remote control of single-cell functions,[8,9] plasmonic devices,[10] and hyperthermia therapy of cancer[11,12] and other diseases.[8] To be effective, local heating requires measuring the nanoheater's local temperature. Notwithstanding great activity in the past decade, sensitive and efficient nanoparticles embedding both heaters and thermometers have not yet been realized, despite several intriguing reports, particularly in the last year.[13−20]

This work develops heating and thermometry in a single nanoparticle with unprecedented thermal contact (the thermometer is located just on the surface of the heater) and explores a glimpse of the possibilities opened by such nanoparticles, a tool that could give a definitive impulse to an effective use of local heat generation at the nanoscale. Simple experiments performed with these nanoparticles with high time (up to 0.250 s) and temperature

* Address correspondence to
lcarlos@ua.pt,
amillan@unizar.es.

Received for review January 5, 2015
and accepted February 18, 2015.

10.1021/acsnano.5b00059

resolutions (0.5 K) show a quasi-instantaneous onset of temperature gradient from the nanoheater to the medium that implies a huge heat resistance that cannot be explained from the macroscopic thermal properties of the system. Moreover, the nanoparticles offer additional advantages, such as an optical thermometric readout, allowing an easy implementation in a large variety of systems, a high stability in aqueous medium, and a capacity for biological multifunctionalization and targeting (Supplementary Section 1).

The heater/thermometer nanoplatform here proposed can be beneficial in many technological applications from microelectronics to bio- and nanomedicine, namely, in hyperthermia. Current strategies for hyperthermia include heating the whole tumor tissue above 315−316 K by radio frequency electromagnetic fields, UV−visible−IR radiation, and ac magnetic fields, using, respectively, dielectric, photonic, and magnetic micro/nanomaterials acting as heat sources. While light-induced approaches are suitable for near-surface applications, the use of magnetic fields allows in-depth applications, now in phase II clinical applications.[11] However, to achieve 315−316 K at the tumor mass, a high load of magnetic nanoparticle is needed. The efficacy of this technique will be much improved when the heat is applied at localized targeted sites in the cells, causing a similar death effect with a much smaller number of nanoparticles.[12] The question then is how high the local temperature can rise before the heat generated by the nanoparticles is dissipated to the medium. This is where the incorporation of local thermometry to the nanoheater will provide the answer. The accurate measurement of the nanoheater's surface temperature by a nanothermometer is crucial for regulating the heat released to the surroundings, allowing the adjustment of the irradiation parameters and thus assisting the therapy.

Progress in the measurement of the nanoheater's temperature followed two directions: (i) using a second nanoparticle for thermometry (dual-particle approach) and (ii) anchoring a molecular thermometric probe at the surface or outer shell of the nanoheater (single-particle approach).

In contrast with strategy (ii), the dual-particle approach has the inherent limitation of the uncontrolled spatial distribution of nanoheaters and nanothermometers,[15−18,21] with the concomitant large distribution of the nanoheater/nanothermometer distances (thermal sensing is not achieved at the same heating volume). These restrictions were partially mitigated recently *via* strategy (ii) by encapsulating magnetic nanoparticles and thermometric luminescent $NaYF_4$:Yb,Er nanoparticles in a larger mesoporous silica nanoparticle.[18] Still, the determination of the heater's temperature was indirect, as the thermometer was 8−9 nm from the heater, and the low temporal resolution (30 s) precluded a fine screening of the heat transfer process. In another (ii) work, Gd_2O_3:Yb,Er nanorods (thermometers) are decorated with Au nanoparticles (heaters).[16] This single integrating nanoplatform has the advantage of measuring the absolute local temperature of the sample volume under irradiation (rather than an average temperature, as in (i)), over a wide range (300 to 2000 K). It has, however, two important disadvantages: the thermometric probe is overdimensioned relative to the heater, and the plasmonic-induced heating power is low because the excitation wavelength required to excite the thermometer (980 nm) is off resonance with the localized surface plasmonic band of the Au NPs (maximum at ∼550 nm).

An early example following the single-particle strategy was performed on Au nanoparticle suspensions using intense pulse lasers (15×10^{-6} J/pulse) for heating and pump−probe spectroscopy for thermometry.[22] This system has an important limitation since heating and temperature measurements are discontinuous, occurring in a very short time scale ($\sim 10^{-10}$ s). In a second example, a fluorophore was attached to the shell of the magnetic heater by a bond that breaks at a certain temperature.[13] An analysis of the fluorophore content in the supernatant after heating gives the moment at which the bond-breaking temperature is reached, but this is still far from a real time and continuous temperature readout. This system was soon improved by using the denaturalization of DNA strands as the temperature probe[14] instead of bond breaking, but still the temperature reading was neither continuous nor instantaneous. A third example uses LaF_3 nanoparticles doped with a high Nd^{3+} concentration (25 at. %) behaving as heaters/thermometers with $0.2\% \cdot K^{-1}$ sensitivity and a heating performance from room temperature to ∼320 K with a high laser power density (up to $3\ W \cdot cm^{-2}$).[19] The same group reported a step forward toward nanoparticle-based photothermal therapy at clinical level, applying the LaF_3:Nd^{3+} (5.6 at. %) nanoparticles to temperature-controlled photothermal therapy of cancer tumors in mice.[20]

RESULTS AND DISCUSSION

The heater/thermometer nanoplatform was prepared from iron oxide cores functionalized with Eu^{3+} and Tb^{3+} complexes, coated with a P4VP-*b*-P(PMEGA-*co*-PEGA) copolymer and dispersed in water to obtain an aqueous ferrofluid suspension (Supplementary Scheme 1, Table 1, Figures 1−8). At neutral pH, the copolymer has a hydrophobic part (P4VP) and a hydrophilic part (PEG) that is well solvated by water molecules, thus restraining the agglomeration of the nanoparticles. Consequently, the ferrofluid suspension is stable for months, as described in the Supporting Information. P4VP-PEGA copolymer coatings have also shown to be advantageous in terms of blood and cell toxicity, as explained in the Supporting Information (Section 1.3). Before use, the ferrofluid was filtered

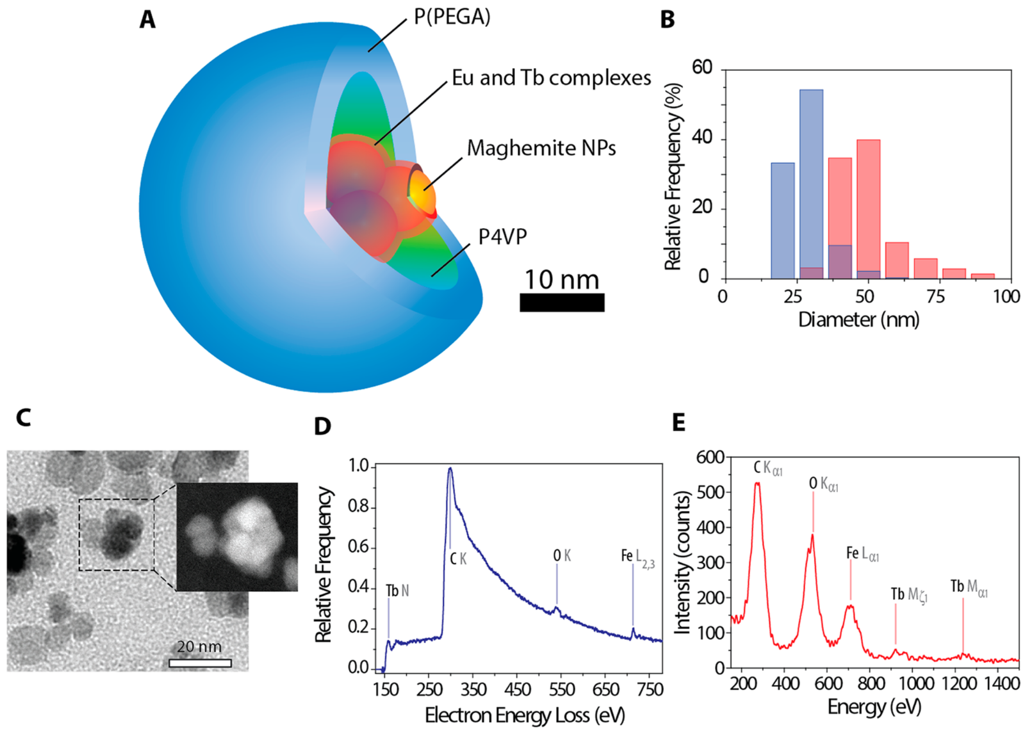

Figure 1. Structural properties of the maghemite multiparticle core—shell beads. (A) Schematic scaled representation of a typical bead. In the central region, the Eu^{3+}/Tb^{3+} complexes (reddish layer) for temperature measurement cover the maghemite NPs (orange). The P4VP (green) forms a first shell encapsulating the magnetic NPs, and the P(PMEGA-*co*-PEGA) chains (blue) occupy the outer part of the bead. (B) Hydrodynamic size distribution of the maghemite multiparticle core (blue bars) and of the whole bead (red bars). (C) TEM/STEM image of the beads showing the multiparticle iron oxide core and chemical image of the sample by STEM showing that all the heavy elements are located in the core. (D) EEL spectrum and (E) EDX spectrum at a point inside the multiparticle core.

(through a 2.2×10^{-7} m filter, so it can be easily sterilized for biological use) and purified by magnetic separation to ensure that all the heater/thermometer nanoplatforms (also called beads throughout the article) contain both the thermometric and magnetic components.

Chemical analysis, scanning transmission electron microscopy (STEM) and cryoTEM (Figure 1C, Supplementary Figures 9, 10), electron diffraction (Supplementary Figure 9), electron energy loss spectroscopy (EELS) (Figure 1D), energy-dispersive spectroscopy (EDX) (Figure 1E, Supplementary Figures 11 and 12), and dynamic light scattering (DLS) (Figure 1B, Supplementary Figure 13) permit building up a structural model of the heater/thermometer bead (Figure 1A). Accordingly, TEM images (Supplementary Figures 9 and 10) show the magnetic multiparticle core has an average diameter $D_c = 23 \pm 9$ nm and is formed by an aggregate of 1 to 7 iron oxide magnetic nanoparticles with a spinel crystal structure and a nanoparticle diameter $D_p = 10 \pm 2$ nm. The DLS results for the size of the magnetic multiparticle core, $D_c = 23.2$ nm (with a polydispersity index, PDI, of 0.3) are very similar to those observed in cryoTEM images (Figure 1B). The polymer shell did not yield any contrast in TEM and cryo-TEM images (Figure 1C); thus the outer diameter of the beads was established from DLS measurements as $D_b = 48.0$ nm (PDI = 0.2, Figure 1B). A key point in this nanoplatform is the location of the thermometric Eu^{3+} and Tb^{3+} ions. A first indication is given by STEM images (Figure 1C, Supplementary Figure 12), showing that bright heavy elements (Fe from the magnetic multiparticle core, Eu and Tb from the complexes) are concentrated in the same regions. Furthermore, EELS and EDX analyses confirmed a co-localization of Fe and Tb (Eu is too scarce to be detected, Supplementary Figure 11) in the bead multiparticle core. EDX analyses at points outside the bead multiparticle core confirm the absence of these elements (Supplementary Figure 12). Therefore, the thermometric Eu^{3+} and Tb^{3+} ions are located on the surface of the iron oxide nanoparticles.

The absolute local temperature is inferred through the dependence on temperature of the emission spectra of the nanoplatform (Figure 2), as reported previously for Eu^{3+}/Tb^{3+}-containing organic—inorganic hybrids.[3,23−25] The thermometric response of such systems results from thermally activated energy transfer between Eu^{3+}- and Tb^{3+}-emitting levels and triplet energy states of the ligands and of the host matrix,[25] resulting in both the temperature range of maximum sensitivity and excitation wavelength capable of being tuned by a proper selection of organic ligands and host matrix.[23,25] In this case the

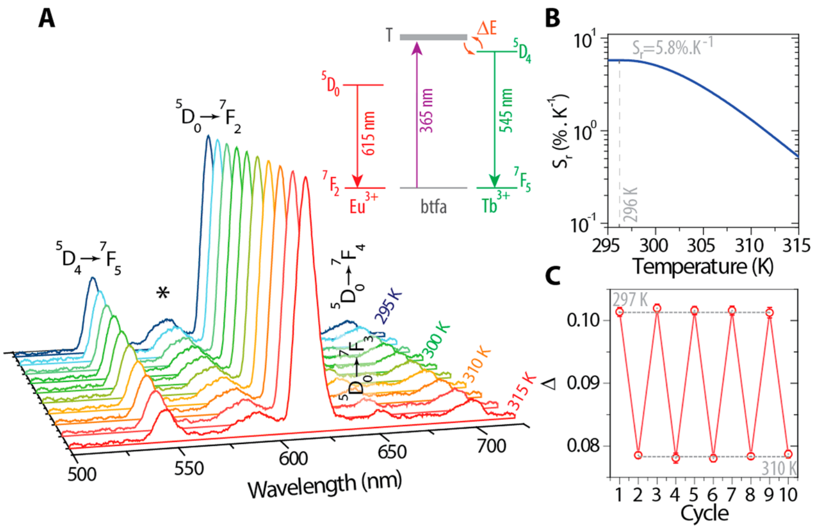

Figure 2. Emission spectra and thermometric performance of the multicore beads. (A) Emission spectra of the water suspension multicore beads (6.2 g $Fe_2O_3 \cdot L^{-1}$) in the temperature range 295–315 K. The excitation wavelength is 365 nm. The $^5D_0 \rightarrow {}^7F_{2-4}$ (Eu^{3+}) and the $^5D_4 \rightarrow {}^7F_5$ (Tb^{3+}) transitions are identified, and the asterisk marks the spectral region where an overlap is observed between the $^5D_0 \rightarrow {}^7F_{0,1}$ and the $^5D_4 \rightarrow {}^7F_4$ lines. The inset shows a simplified energy scheme of the Eu^{3+} and Tb^{3+} ions and btfa ligand, where the most intense Eu^{3+} and Tb^{3+} transitions are presented. The orange arrows represent the thermally driven $^5D_4 \rightarrow$ host energy transfer and the corresponding back transfer. (B) Relative sensitivity S_r of the water suspension multicore beads in the temperature range 295–315 K. (C) Temperature cycling of the water suspension multicore beads between 297 and 310 K, with a repeatability better than 99.5% in the 10 consecutive cycles. The solid and interrupted lines are guides for the eyes. The error bars result from the standard deviation of each histogram (60 s acquisition).

nanothermometer was designed using Eu^{3+} and Tb^{3+} ions, btfa (4,4,4-trifluoro-1-phenyl-1,3-butanedione) ligands, and P4VP, aiming for an optimal sensitivity at the physiological temperature range and a cost-effective 365 nm excitation wavelength (Supplementary Figures 14–20). The emission spectra of the water suspension of the beads shows that the $^5D_0 \rightarrow {}^7F_2$ (Eu^{3+}) integrated intensity (I_{Eu}) is insensitive to temperature, whereas the intensity of the $^5D_4 \rightarrow {}^7F_5$ (Tb^{3+}) transition (I_{Tb}) decreases with the temperature increase (Figure 2A). This temperature dependence is rationalized assuming that the first excited triplet state of the btfa ligand with energy above that of the $^5D_4$ emitting state is populated through thermally driven Tb^{3+}-to-ligand energy transfer (diminishing, therefore, the $^5D_4 \rightarrow {}^7F_5$ intensity). The energy difference between that triplet state and the $^5D_0$ emitting level is too large to permit the thermally driven depopulation of the Eu^{3+} emitting state in the 295–315 K interval, and the thermometric parameter $\Delta = I_{Tb}/I_{Eu}$ guarantees the absolute measurement of temperature.[25] The ratiometric thermometric parameter Δ allows the emission spectrum/temperature conversion through the calibration curve generated for the particular experimental conditions used (Supplementary Table 2, Figure 21A).

As discussed elsewhere,[3] the ratiometric (or self-referencing) intensity measurements are not compromised by the well-known disadvantages of experiments based on the intensity of only one transition. The thermometric performance of the beads is evaluated using the relative sensitivity $S_r = (\partial\Delta/\partial T)/\Delta$,[3,23] ranging from 0.5 to 5.8%·K^{-1}, 295–315 K (maximum sensitivity of 5.8%·K^{-1} at 296 K, Figure 2B). No hysteresis and/or photobleaching distorting temperature measurements are discernible in the time scale of the experiments (Figure 2). Upon 10 consecutive temperature cycles between 297 and 310 K, the thermometer reproducibility is as high as 99.5% (Figure 2C), demonstrating the robustness of the temperature readout. In our experimental conditions, the time fluctuations of the thermometric parameter Δ are always below 0.7%, decreasing when the integration time is increased. Converting these fluctuations into temperature allows one to calculate the uncertainty of the temperature measurement, which is 0.5 K (Supplementary Figure 21B).

The heater/thermometer nanoplatform is applied to monitor local temperature changes under ac magnetic fields (Figure 3). A scheme of the experimental setup used is depicted in Figure 3A (Supplementary Scheme 2). Two on–off field protocols are described, illustrating a classic one-pulse protocol (Figure 3B) and a multiple-pulse protocol where the fine heating–thermometry ability of the beads is highlighted (Figure 3C,D, Supplementary Figure 22). For comparison purposes, temperature readings through a semiconductor optical reference thermometer immersed in the fluid and an infrared thermal camera focused on the wall of the container are also used. As expected, before the field was turned on, temperature values in all thermometers were coincident and constant (Figure 3B–D).

When the field was switched on, the molecular thermometer responded immediately and with a quite sharp slope, while the semiconductor thermometer

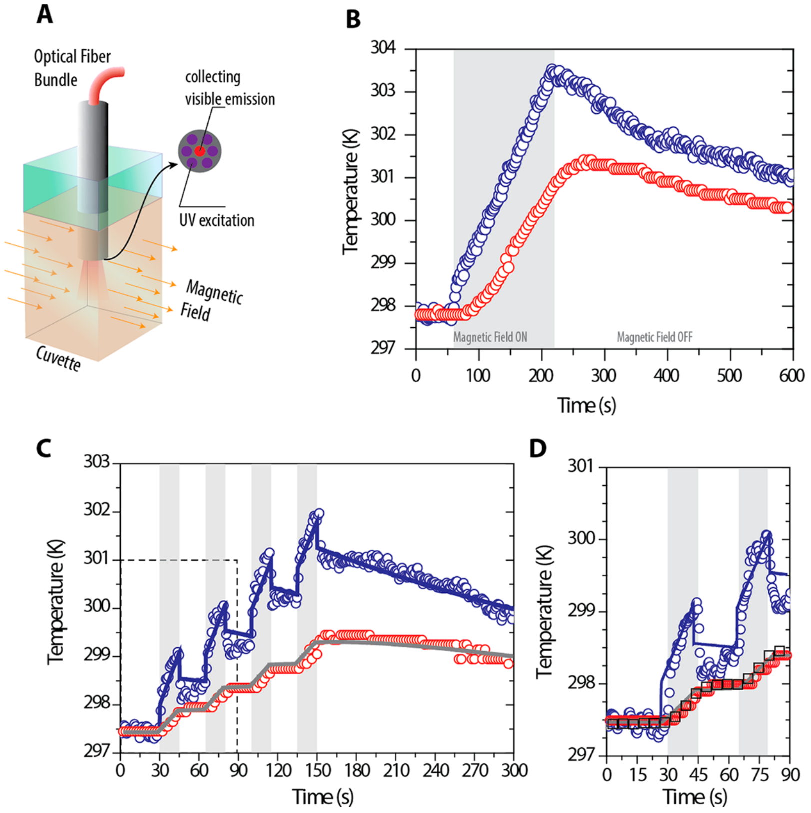

Figure 3. Temperature dynamics during the on–off switching of an ac magnetic field. (A) Schematic representation of the experimental setup showing the cuvette filled with the water-suspended multicore beads and the optical fiber bundle, composed of 1 core fiber for emission recovery and 6 lateral fibers for excitation (fiber diameter of 400 × 10^{-6} m). (B) Temperature measurement of a 0.75 mL ferrofluid suspension during a 600 s one-pulse experiment using the molecular (blue circles) and semiconductor (read circles) thermometers. The shadowed area marks the time interval when the magnetic field is turned on (60–220 s). (C) Temperature measurement of the same suspension during a 300 s multipulse experiment using the molecular (blue circles) and semiconductor (red circles) thermometers. The shadowed areas mark the time intervals when the magnetic field is turned on (15 s). The solid lines correspond to the fit of experimental data with the lumped elements model (Schemes S3–S5). (D) Zoom of the first 90 s of the measurements (marked area in part C). For comparison, the infrared thermal camera (black squares) temperature readout is included.

had a delay of about 10 s and a smoother slope. Similarly, when the field is switched off, the response of the molecular thermometer is again faster and sharper than that of the semiconductor thermometer (Figure 3B–D), converging then for longer times (Supplementary Figure 22A). Clearly, the most interesting thermal events occur during 15 s after switching the field on and off, and they can be discerned only when the time response of the thermometer is fast, as is the case here (characteristic time, at least, on the order of the detector integration time, 0.250 s). Besides the necessary high temporal resolution, the observation of the sharp features for $t < 10$ s is expected only if the system has a good thermal conductivity and a small heat capacity between the heat source and the thermometer. This is a signature of a thermometer truly coupled to a heat source, and, to the best of our knowledge, it is the first time that such a signature is found for heat sources of such small size. The time response of the heater/thermometer nanoplatform reported here is much faster when compared with the thermometers that are coupled with heat sources, *e.g.*, 2 orders of magnitude higher than the only value reported so far, 30 s for magnetically heated nanoparticles.[18] However, there are examples of nanothermometers demonstrating faster response, *e.g.*, the *in vitro* nonratiometric temperature measurements with a temporal resolution of 10^{-2} s.[26]

The temperature variation at the nanoheater and its temperature gap with the surrounding media presented here are in consonance with previous findings[9,13,18] and deserve a critical look. With this purpose, we focus our attention on one single bead (Figure 1A) surrounded by water. The expected power dissipated by each heater, $P \approx (7-10) \times 10^{-16}$ W/bead, is estimated based on the out-of-phase component of the ac magnetic susceptibility (Supplementary Figures 23–25). This value corresponds to a specific power loss of 33 to 50 W/g (Fe_2O_3), which is within the range of those usually found for Fe_2O_3 nanoparticles.[27] Naturally, this power results in a heat flux and in a temperature gradient, whose values depend on the thermal properties of the polymer coating, water, and the container. On the basis of the P4VP and P(PEGA) bulk thermal conductance (and for a coating with a thickness of ∼13 nm), the temperature gradient across the polymers is expected to be on the order of 10^{-8} K. Then, no temperature gap between the nanoparticles and the water should be observed (Supplementary Tables 3 and 4 for dimensions and macroscopic thermal parameters of the materials).

Currently, it is not yet clear whether an increasing number of experimental results[9,13,15,18,28] (including those reported here) are meaningless or whether the macroscopic models/parameters applied to the nanoheaters are not valid. Evidence for the existence of large temperature gaps between nanoheaters and surrounding media comes from different heating sources (*i.e.*, magnetothermia,[9,13,18] absorption/dissipation by Au nanoparticles,[21] and nonradiative decay in LaF_3:Nd^{3+} nanoparticles[19]) and different thermometric systems (*i.e.*, Au nanoparticles, quantum dots, proteins, nanodiamonds, and trivalent lanthanide ions). These systems have so far passed the most obvious reliability tests under different chemical environments and external fields,[28] and they not contradict the thermodynamic arguments presented by Baffou *et al.*[29] demonstrating the impossibility of having temperature heterogeneities of up to a few Kelvins inside a single cell resulting from internal energy dissipation mechanisms (endogenous thermogenesis). We also notice that the application of an ac magnetic field to cells containing a small number of magnetic nanoparticles induces cell death without increasing the global cell temperature.[30] This may be taken as indirect evidence of local temperature gaps like the one measured in the present experiments. Concerning the models/parameters applied to the nanoheaters, it has been pointed out that nanoparticles behave very differently when compared to bulk systems.[1] For instance, the emergence of a resistance for the heat transport at the nanointerfaces induces the appearance of temperature gradients.[31,32] Interphase heat resistances are usually given as the equivalent thickness of an extra layer of material producing the same effect (Kapitza length, l_K). In our case l_K is on the order of 20 nm, which means that the overall thermal resistance would increase by an order of magnitude at most with respect to heat transfer across the polymer shell (Supplementary Section 7).

An estimation of the equivalent thermal parameters needed to reproduce the experimental results under the classical heat laws can be obtained by considering a lumped thermal capacity model, based on a simplification of the structural model of Figure 1 (Supplementary Schemes 4, 5). This approach is justified since a uniform temperature within each element of the bead is expected based on the estimated Biot number (Supplementary Section 7.6). The model consists of a heat source simulating the heat dissipated by the iron oxide nanoparticles, the heat capacitances of a (lumped) polymer coating, the water and the wall of the container, and thermal resistances between each element and between water and air and the wall and air (Supplementary Scheme 5). The best fit is shown in Figure 3C,D and in Supplementary Figure 26, using the effective lumped resistances presented in Supplementary Table 5. As expected, given the relation between the capacitance of the polymer and water, the temperature at the polymer (where the molecular thermometer is placed) follows the jumps of the heating source. The measurement of the semiconductor thermometer is close to the measurement of the infrared camera at the surface of the wall of the container (Figure 3D), which is well reproduced by the simulation.

While the heat capacitances of the ∼10^{17} beads (present in the ferrofluid suspension) are close to those expected from bulk, the equivalent thermal resistances are 10 orders of magnitude higher than those predicted using the bulk thermal conductivity and the bead dimensions (Supplementary Section 7), stressing the profound contradiction between models and experimental results aforementioned.

Opossum kidney (OK) cells were incubated with the heater/thermometer nanoparticles. Fluorescence images under UV excitation (340–380 nm) were taken simultaneously after half-splitting the emission in two separate wavelength ranges covering the main emission bands of Tb^{3+} (529–555 nm) and Eu^{3+} (597–620 nm) (Figure 4). Observation (through the ocular lenses) of cells stained with DAPI showed the internalization of the nanoparticles, mostly around the nucleus, although it seems they have not penetrated inside (Supplementary Section 8). A comparison of Figure 5A,B unequivocally shows the co-localization of both Tb^{3+} and Eu^{3+} ions in the OK cells over a region near the nucleus. This enables the thermometric mapping at subcellular scale by simply taking the pixel-by-pixel ratio of the Tb^{3+} and Eu^{3+} intensities and using the calibration curve of Supplementary Figure 21A. Figure 5C shows a temperature mapping of the regions of interest (where both emissions are discernible), permitting estimating the temperature near the cell's nucleus. The histogram of Figure 5D indicates that the temperature is constant over the region mapped (299.3 ± 0.2 K) within the uncertainty of the molecular thermometer (0.5 K). The maps of two other imaged nuclei (squares 2 and 3 in Figure 4C,D) reveal a temperature distribution similar to that of square 1 (Supplementary Figure 27), despite the changes on the intensity values of the Tb^{3+} and Eu^{3+} emissions. The lateral resolution of such mapping is defined by the pixel image and corresponds to ∼220 nm. The penetration depth of the UV-excited heater/thermometer nanoplatforms reported here is estimated as ∼0.2×10^{-3} m.[33] Although the penetration depth could be improved by shifting the excitation to the NIR spectral range,[34,35] the thermal

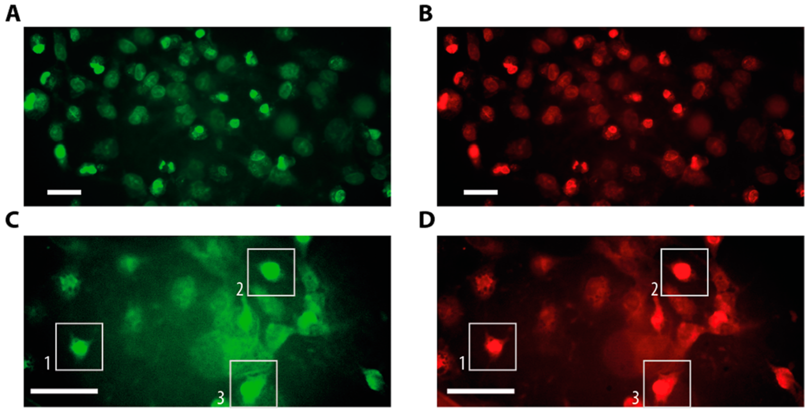

Figure 4. Imaging of Tb^{3+} and Eu^{3+} emissions from cell-internalized multicore beads. Fluorescence images of OK cells treated with the nanoparticles showing the Tb^{3+} (545 nm) (A and C) and Eu^{3+} (610 nm) (B and D) emissions. The brightness and colors have been modified for better visualization and do not correspond to the actual intensity ratio. All scale bars correspond to 40 μm.

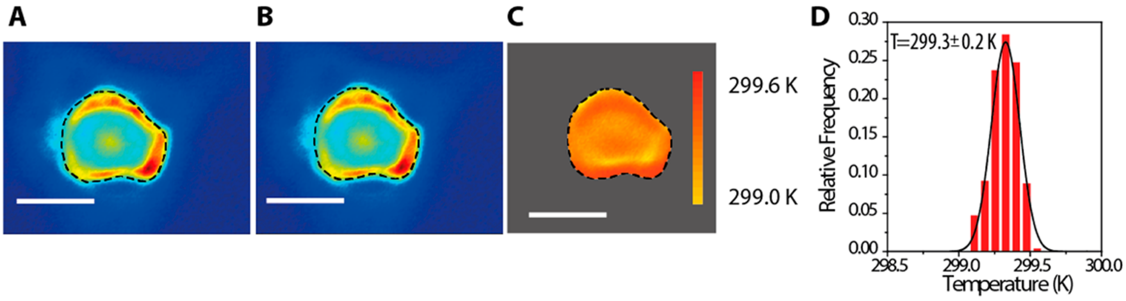

Figure 5. Temperature mapping of OK cells. Magnification of the areas in Figure 4C,D delimited by the squares showing the (A) Eu^{3+} ($^5D_0 \rightarrow {}^7F_2$, 610 nm) and (B) Tb^{3+} ($^5D_4 \rightarrow {}^7F_5$, 545 nm) emissions. The pseudocolored maps were chosen to illustrate the co-localization of the Eu^{3+} and Tb^{3+} emissions. For better visualization, the maximum of the Tb^{3+} colormap was scaled by a factor of 3. The interrupted lines delimitate the nucleus of the OK cell, marking the region of interest where the temperature map presented in part C was computed. (D) The histogram of the temperature distribution near the OK nucleus follows a Gaussian distribution of mean value (±standard deviation) 299.3 ± 0.2 K ($r^2 > 0.997$), in accord with the cell culture temperature. All scale bars correspond to 10 μm.

sensitivity is, in general, poorer. For instance, in Nd^{3+}-doped luminescent thermometers with NIR excitation and emission (within the first biological optical window) the relative sensitivity is almost 40 times lower that that reported here, despite the much larger penetration depth, $\sim(1-2) \times 10^{-3}$ m.[34,35] However, NIR excitation is less damaging to cells compared with UV excitation (especially when high-power densities are used), and the signal measurements are not disturbed as much by tissue autofluorescence as UV-excited signals.

CONCLUSIONS

In summary, the unprecedented relatively small heat capacitance of the molecular thermometer and its physical contact with the nanoheaters reveal the existence of an unexpected temperature gradient between nanoheaters and surrounding media for relatively long time intervals ($t > 10$ s) and relatively low heat powers (10^{-16} W/heater). Moreover, the continuous temperature monitoring with high time resolution allows the observation of previously undisclosed changes during the first few seconds ($t < 10$ s) of heating by an ac magnetic field. This opens intriguing possibilities in studies of the heat flow at the nanoscale, including thermal capacitance and conductivity across nanostructured media,[36] as for instance detailed studies in cellular thermal processes.[37,38] In addition, we have established the local temperature mapping near the nucleus of OK cells incubated with the heater/thermometer beads simply using the pixel-by-pixel ratio of the Tb^{3+} and Eu^{3+} intensities. Furthermore, the heater/thermometer single nanoplatform reported here shows great potential for the magnetically triggered gene expression control that resulted in tumor growth inhibition[39] and for impact on the design of hyperthermia therapies based on localized manipulation of heat flows and short application times. In this way, local energy supply that is not immediately dissipated to the surrounding media could be enough to induce irreversible intracellular damage in tumor cells within a short time period, while maintaining the temperature of the neighboring tissue.[40] Together with an adequate vectorization of the particles, unprecedented specificity would be achieved. The use of the system presented here can help to settle these questions and to give a fair account of the real potential of local hyperthermia. In a more extended vision, accurately controlled local heating and precise temperature determination in the cellular media will enable thermal conductivity studies in cellular organelles and across membranes, as well as detailed studies in cell physiology related to thermal processes.

METHODS

Synthesis. All the synthetic procedures are described in detail in Supplementary Section 1. P4VP-Cl and the final diblock copolymer P4VP-*b*-P(PMEGA-*co*-PEGA) were prepared by atom transfer radical polymerization. [Ln(btfa)$_3$(H$_2$O)$_2$] (Ln = Eu, Tb) complexes were prepared by mixing the reactants in ethanol solutions. Iron oxide multiparticle cores were prepared by precipitation of iron salts in ammonia solutions. Core−shell Eu^{3+}/Tb^{3+}-containing Fe$_2$O$_3$@P4VP-*b*-P(MPEGA-*co*-PEGA) nanoparticles were prepared by addition of the polymer to an acidic suspension of iron oxide nanoparticles, increasing the pH to 7.4, and addition of ethanol solutions of the two lanthanide complexes. The suspension was filtered (0.22 μm), and the nanoparticles were collected by magnetic separation and resuspended in water to obtain the final ferrofluid.

Composition and Structure Characterization. The Fe, Tb, and Eu contents in the Eu^{3+}/Tb^{3+}-containing Fe$_2$O$_3$@P4VP-*b*-P-(MPEGA-*co*-PEGA) nanoparticles were determined by coupled plasma atomic emission spectrometry (ICP-AES). TEM observations were carried in a JEOL 2000-FXII microscope equipped with EDX analyzer, and STEM and cryo-TEM observations were performed in a FEI Tecnai F30 microscope equipped with both EELS and EDX analyzers. Dynamic light scattering measurements were performed in a Zetasizer Nano ZS from Malvern Laser (see Supplementary Section II).

Magnetic Heating Equipment. A homemade magnetic heating source was used consisting of a signal generator, a high-power amplifier, and a matching transformer connected to an *RCL* circuit. The magnetic field produced at the *L* element consists of low-inductance Litz wires around a ferrite nucleus with a section of 3 × 2.7 cm and a gap of 1 cm where the sample is placed. The field intensity and frequency during the measurements were 23 mT and 97.771 kHz, respectively (Supplementary Section 6.1).

Optical Characterization. Photoluminescence spectra of Eu^{3+} and Tb^{3+} complexes encapsulated in the block copolymer were obtained at room temperature by exciting the samples with a 1000 W ORIEL 66187 tungsten halogen lamp and a double 0.22 m SPEX 168OB monochromator. Fluorescence emission was detected using a 0.5 JAREL-ASH monochromator with a Hamamatsu R928 photomultiplier tube. All optical spectroscopy measurements were corrected from the system response. The spectra of the Eu^{3+}/Tb^{3+}-containing Fe$_2$O$_3$@P4VP-*b*-P-(MPEGA-*co*-PEGA) nanoparticles were recorded with a modular double grating excitation spectrofluorimeter with a TRIAX 320 emission monochromator (Fluorolog-3, Horiba Scientific) coupled to an R928 Hamamatsu photomultiplier, using a front face acquisition mode. The excitation source was a 450 W Xe arc lamp. The emission spectra were corrected for detection and optical spectral response of the spectrofluorimeter, and the excitation spectra were corrected for the spectral distribution of the lamp intensity using a photodiode reference detector. The emission decay curves were measured with the setup described for the luminescence spectra using a pulsed Xe−Hg lamp (6×10^{-6} s pulse at half-width and $(20-30) \times 10^{-6}$ s tail).

Time-Resolved Nanothermometry. The setup used to perform time-resolved nanothermometry of the Eu^{3+}/Tb^{3+}-containing Fe$_2$O$_3$@P4VP-*b*-P(MPEGA-*co*-PEGA) nanoparticles in a water suspension consists of an excitation high-power LED light source (LLS-365, Ocean Optics, centered at 365 nm) connected to the outer fiber bundle (modified Ocean Optics QR450-7-XSR fiber with a polyether ether ketone housing instead of the usual metallic one). The emission is collected by the central fiber and measured with a USB-4000FL portable spectrometer (Ocean Optics), controlled by MatLab routines (Supplementary Scheme 2).

Cell Observations. OK cells (a cell model of proximal tubular renal cells from American opossum) were kindly provided by Dr. V. Sorribas (U. Zaragoza) and were grown in Dulbecco's modified Eagle's medium-Ham's F12 (Gibco-Life Technologies), supplemented with 10% fetal calf serum (FCS), glutamine, and antibiotics. The cells were made quiescent for 24 h previous to the treatments with ferrofluids by incubating them in the same medium containing only 0.5% FCS. For fluorescence observations, quiescent cells grown in chamber slides (Millipore) were treated with thermometric nanoparticles for an additional 24 h. Then, the supernatants were aspirated out, and the cells were washed three times with cold PBS, fixed with 3% (w/v) paraformaldehyde for 10 min, washed again three times, and mounted for microscopy. Control cell cultures were also grown in the absence of the ferrofluid. A series of samples were stained with DAPI for the localization of cell nuclei. Fluorescence microscope observations were carried out in a Leica DMI3000B inverted microscope under 340−380 nm excitation light. The images were taken in an Orca 4.0 camera coupled to a Gemini beam splitter, both from Hamamatsu.

Conflict of Interest: The authors declare no competing financial interest.

Supporting Information Available: Detailed materials and methods, as well as additional experimental data (Figures S1−S27). This material is available free of charge *via* the Internet at http://pubs.acs.org.

Acknowledgment. This work was partially supported by the Spanish Ministry of Science and Innovation (MAT2011-259911) and in part developed in the scope of the project CICECO-Aveiro Institute of Materials (ref. FCT UID/CTM/50011/2013), financed by Portuguese funds through the FCT/MEC (RECI-CTM-CER-0336-2012, EXPL-CTM-NAN-0295-2012) and when applicable cofinanced by FEDER under the PT2020 Partnership Agreement. C.D.S.B. (SFRH/BPD/89003/2012) and N.J.O.S. acknowledge FCT for a postdoctoral grant and an IF 2013 contract, respectively. R.B. thanks ICMA-CSIC for a JAE-predoc grant. The authors would like to acknowledge the use of Servicio General de Apoyo a la Investigación-SAI, Universidad de Zaragoza.

REFERENCES AND NOTES

1. Cahill, D. G.; Braun, P. V.; Chen, G.; Clarke, D. R.; Fan, S. H.; Goodson, K. E.; Keblinski, P.; King, W. P.; Mahan, G. D.; Majumdar, A.; *et al.* Nanoscale Thermal Transport. II. 2003−2012. *Appl. Phys. Rev.* **2014**, *1*, 011305.
2. Wang, X. D.; Wolfbeis, O. S.; Meier, R. J. Luminescent Probes and Sensors for Temperature. *Chem. Soc. Rev.* **2013**, *42*, 7834–7869.
3. Brites, C. D. S.; Lima, P. P.; Silva, N. J. O.; Millán, A.; Amaral, V. S.; Palacio, F.; Carlos, L. D. Thermometry at the Nanoscale. *Nanoscale* **2012**, *4*, 4799–829.
4. Okabe, K.; Inada, N.; Gota, C.; Harada, Y.; Funatsu, T.; Uchiyama, S. Intracellular Temperature Mapping with a Fluorescent Polymeric Thermometer and Fluorescence Lifetime Imaging Microscopy. *Nat. Commun.* **2012**, *3*, 705.
5. Jaque, D.; Vetrone, F. Luminescence Nanothermometry. *Nanoscale* **2012**, *4*, 4301–4326.
6. Mura, S.; Nicolas, J.; Couvreur, P. Stimuli-Responsive Nanocarriers for Drug Delivery. *Nat. Mater.* **2013**, *12*, 991–1003.
7. Baffou, G.; Quidant, R. Thermo-Plasmonics: Using Metallic Nanostructures as Nano-Sources of Heat. *Laser Photonics Rev.* **2013**, *7*, 171–187.
8. Stanley, S. A.; Gagner, J. E.; Damanpour, S.; Yoshida, M.; Dordick, J. S.; Friedman, J. M. Radio-Wave Heating of Iron Oxide Nanoparticles Can Regulate Plasma Glucose in Mice. *Science* **2012**, *336*, 604–608.
9. Huang, H.; Delikanli, S.; Zeng, H.; Ferkey, D. M.; Pralle, A. Remote Control of Ion Channels and Neurons through

Magnetic-Field Heating of Nanoparticles. *Nat. Nanotechnol.* **2010**, *5*, 602–606.

10. Schuller, J. A.; Barnard, E. S.; Cai, W. S.; Jun, Y. C.; White, J. S.; Brongersma, M. L. Plasmonics for Extreme Light Concentration and Manipulation. *Nat. Mater.* **2010**, *9*, 193–204.
11. Thiesen, B.; Jordan, A. Clinical Applications of Magnetic Nanoparticles for Hyperthermia. *Int. J. Hyperther.* **2008**, *24*, 467–474.
12. Reddy, L. H.; Arias, J. L.; Nicolas, J.; Couvreur, P. Magnetic Nanoparticles: Design and Characterization, Toxicity and Biocompatibility, Pharmaceutical and Biomedical Applications. *Chem. Rev.* **2012**, *112*, 5818–5878.
13. Riedinger, A.; Guardia, P.; Curcio, A.; Garcia, M. A.; Cingolani, R.; Manna, L.; Pellegrino, T. Subnanometer Local Temperature Probing and Remotely Controlled Drug Release Based on Azo-Functionalized Iron Oxide Nanoparticles. *Nano Lett.* **2013**, *13*, 2399–2406.
14. Dias, J. T.; Moros, M.; del Pino, P.; Rivera, S.; Grazu, V.; de la Fuente, J. M. DNA as a Molecular Local Thermal Probe for the Analysis of Magnetic Hyperthermia. *Angew. Chem., Int. Ed.* **2013**, *52*, 11526–11529.
15. Maestro, L. M.; Haro-González, P.; Iglesias-de la Cruz, M. C.; Sanzrodríguez, F.; Juarranz, A.; Solé, J. G.; Jaque, D. Fluorescent Nanothermometers Provide Controlled Plasmonic-Mediated Intracellular Hyperthermia. *Nanomedicine (London, U. K.)* **2013**, *8*, 379–88.
16. Debasu, M. L.; Ananias, D.; Pastoriza-Santos, I.; Liz-Marzan, L. M.; Rocha, J.; Carlos, L. D. All-in-One Optical Heater-Thermometer Nanoplatform Operative from 300 to 2000 K Based on Er^{3+} Emission and Blackbody Radiation. *Adv. Mater.* **2013**, *25*, 4868–4874.
17. Freddi, S.; Sironi, L.; D'Antuono, R.; Morone, D.; Dona, A.; Cabrini, E.; D'Alfonso, L.; Collini, M.; Pallavicini, P.; Baldi, G.; *et al.* A Molecular Thermometer for Nanoparticles for Optical Hyperthermia. *Nano Lett.* **2013**, *13*, 2004–2010.
18. Dong, J.; Zink, J. I. Taking the Temperature of the Interiors of Magnetically Heated Nanoparticles. *ACS Nano* **2014**, *8*, 5199–5207.
19. Rocha, U.; Kumar, K. U.; Jacinto, C.; Ramiro, J.; Caamano, A. J.; Solé, J. G.; Jaque, D. Nd^{3+} Doped LaF_3 Nanoparticles as Self-Monitored Photo-Thermal Agents. *Appl. Phys. Lett.* **2014**, *104*, 053703.
20. Carrasco, E.; del Rosal, B.; Sanz-Rodríguez, F.; de la Fuente, Á. J.; Gonzalez, P. H.; Rocha, U.; Kumar, K. U.; Jacinto, C.; Solé, J. G.; Jaque, D. Intratumoral Thermal Reading during Photo-Thermal Therapy by Multifunctional Fluorescent Nanoparticles. *Adv. Funct. Mater.* **2015**, *25*, 615–626.
21. Kucsko, G.; Maurer, P. C.; Yao, N. Y.; Kubo, M.; Noh, H. J.; Lo, P. K.; Park, H.; Lukin, M. D. Nanometre-Scale Thermometry in a Living Cell. *Nature* **2013**, *500*, 54–58.
22. Hu, M.; Petrova, H.; Hartland, G. V. Investigation of the Properties of Gold Nanoparticles in Aqueous Solution at Extremely High Lattice Temperatures. *Chem. Phys. Lett.* **2004**, *391*, 220–225.
23. Brites, C. D. S.; Lima, P. P.; Silva, N. J. O.; Millán, A.; Amaral, V. S.; Palacio, F.; Carlos, L. D. A Luminescent Molecular Thermometer for Long-Term Absolute Temperature Measurements at the Nanoscale. *Adv. Mater.* **2010**, *22*, 4499–4504.
24. Brites, C. D. S.; Lima, P. P.; Silva, N. J. O.; Millán, A.; Amaral, V. S.; Palacio, F.; Carlos, L. D. Lanthanide-Based Luminescent Molecular Thermometers. *New J. Chem.* **2011**, *35*, 1177–1183.
25. Brites, C. D. S.; Lima, P. P.; Silva, N. J. O.; Millán, A.; Amaral, V. S.; Palacio, F.; Carlos, L. D. Ratiometric Highly Sensitive Luminescent Nanothermometers Working in the Room Temperature Range. Applications to Heat Propagation in Nanofluids. *Nanoscale* **2013**, *5*, 7572–7580.
26. Oyama, K.; Takabayashi, M.; Takei, Y.; Arai, S.; Takeoka, S.; Ishiwata, S. i.; Suzuki, M. Walking Nanothermometers: Spatiotemporal Temperature Measurement of Transported Acidic Organelles in Single Living Cells. *Lab Chip* **2012**, *12*, 1591–1593.
27. Fortin, J. P.; Wilhelm, C.; Servais, J.; Menager, C.; Bacri, J. C.; Gazeau, F. Size-Sorted Anionic Iron Oxide Nanomagnets as Colloidal Mediators for Magnetic Hyperthermia. *J. Am. Chem. Soc.* **2007**, *129*, 2628–2635.
28. Takei, Y.; Arai, S.; Murata, A.; Takabayashi, M.; Oyama, K.; Ishiwata, S.; Takeoka, S.; Suzuki, M. A Nanoparticle-Based Ratiometric and Self-Calibrated Fluorescent Thermometer for Single Living Cells. *ACS Nano* **2014**, *8*, 198–206.
29. Baffou, G.; Rigneault, H.; Marguet, D.; Jullien, L. A Critique of Methods for Temperature Imaging in Single Cells. *Nat. Meth.* **2014**, *11*, 809–901.
30. Goya, G. F.; Asin, L.; Ibarra, M. R. Cell Death Induced by Ac Magnetic Fields and Magnetic Nanoparticles: Current State and Perspectives. *Int. J. Hyperther.* **2013**, *29*, 810–818.
31. Hu, M.; Keblinski, P.; Schelling, P. K. Kapitza Conductance of Silicon-Amorphous Polyethylene Interfaces by Molecular Dynamics Simulations. *Phys. Rev. B* **2009**, *79*, 104305.
32. Shenogina, N.; Godawat, R.; Keblinski, P.; Garde, S. How Wetting and Adhesion Affect Thermal Conductance of a Range of Hydrophobic to Hydrophilic Aqueous Interfaces. *Phys. Rev. Lett.* **2009**, *102*, 156101.
33. Meinhardt, M.; Krebs, R.; Anders, A.; Heinrich, U.; Tronnier, H. Wavelength-Dependent Penetration Depths of Ultraviolet Radiation in Human Skin. *J. Biomed. Opt.* **2008**, *13*, 044030.
34. Rocha, U.; Jacinto da Silva, C.; Ferreira Silva, W.; Guedes, I.; Benayas, A.; Martínez Maestro, L.; Acosta Elias, M.; Bovero, E.; van Veggel, F. C.; García Solé, J. A.; *et al.* Subtissue Thermal Sensing Based on Neodymium-Doped LaF_3 Nanoparticles. *ACS Nano* **2013**, *7*, 1188–1199.
35. Benayas, A.; del Rosal, B.; Pérez-Delgado, A.; Santacruz-Gómez, K.; Jaque, D.; Hirata, G. A.; Vetrone, F. *Nd:YAG near-Infrared Luminescent Nanothermometers* **2015**, 10.1002/adom.201400484.
36. Costescu, R. M.; Cahill, D. G.; Fabreguette, F. H.; Sechrist, Z. A.; George, S. M. Ultra-Low Thermal Conductivity in W/Al_2O_3 Nanolaminates. *Science* **2004**, *303*, 989–990.
37. Savitski, M. M.; Reinhard, F. B. M.; Franken, H.; Werner, T.; Savitski, M. F.; Eberhard, D.; Molina, D. M.; Jafari, R.; Dovega, R. B.; Klaeger, S.; *et al.* Tracking Cancer Drugs in Living Cells by Thermal Profiling of the Proteome. *Science* **2014**, *343*, 1255784.
38. Saunders, L. R.; Verdin, E. Cell Biology Stress Response and Aging. *Science* **2009**, *323*, 1021–1022.
39. Yamaguchi, M.; Ito, A.; Ono, A.; Kawabe, Y.; Kamihira, M. Heat-Inducible Gene Expression System by Applying Alternating Magnetic Field to Magnetic Nanoparticles. *ACS Synth. Biol.* **2014**, *3*, 273–279.
40. Schroeder, A.; Heller, D. A.; Winslow, M. M.; Dahlman, J. E.; Pratt, G. W.; Langer, R.; Jacks, T.; Anderson, D. G. Treating Metastatic Cancer with Nanotechnology. *Nat. Rev. Cancer* **2012**, *12*, 39–50.